Modeling the Strong Gravitational Lens: SDSS J1438+1454

Sam Dunham

April 27, 2016

A thesis submitted in partial fulfillment of the requirements for the honors Astronomy and Astrophysics Bachelors of Science degree at the University of Michigan 2016

I would especially like to thank my research advisor Dr. Keren Sharon for letting me help her with her research, helping me write this thesis, and helping me in general throughout my time as an undergraduate. I would also like to thank Traci Johnson for helping me with many lens models and helping me hone my lens modeling skills. Finally I would like to thank all the members of the Sloan Giant Arcs Survey (SGAS) collaboration for helping to make this work and thesis possible.

1 Introduction

1.1 Brief History of Lensing

In 1730, Sir Isaac Newton's (1643-1727) fourth volume of Opticks was published [1]. At the end of the volume, Sir Newton set forth several queries, the first of which was, "Do not Bodies act upon Light at a distance, and by their action bend its Rays, and is not this action (cæteris paribus) strongest at the least distance?". Calculating the deflection of light by a point source in Newtonian gravity yields [1]

$$\delta_N = \frac{2GM}{bc^2}, \tag{1}$$

where G is Newton's gravitational constant, M is the mass of the deflecting body, c is the speed of light, and b is the impact parameter of the photon. In 1915, Albert Einstein (1879-1955) published the deflection of light by a point source according to his general relativity in a curved space-time [2], yielding twice the Newtonian value,

$$\delta_{GR} = 2\delta_N = \frac{4GM}{bc^2}. \tag{2}$$

In 1919, Sir Arthur Eddington (1882-1944) measured the deflection of starlight by the sun during a solar eclipse, thereby providing a verification of one of the predictions of Einstein's theory.

1.2 Lensing as a Weight Scale

In 1933, Fritz Zwicky (1898-1974) postulated the existence of dark matter when he was examining the Coma cluster [3]. Four years later he extended the idea to galaxy clusters deflecting light from background sources [3]. Since the location of the lensed images depends on the mass of the deflecting object (eq (2)), studying the images can be used to measure the mass of the deflecting object. Since then the idea has been extended to measuring the masses of galaxy clusters.

1.3 Lensing as an Extra-Galactic Telescope

In addition to giving a new way to measure astronomical masses, lensing offers a way to see deeper into the universe. Since light is deflected it magnifies the background source, similar to how a magnifying glass works. The magnification boost provided by galaxy clusters can be enough that sources too faint to be seen with today's most powerful telescopes become visible and available for study. This fact is the basis for the collaboration that I am a part of, known as the Sloan Giant Arcs Survey (SGAS) [4–7]. This group is using galaxy clusters as telescopes to study star formation in galaxies at redshift around two [8–12], the epoch at which most of the star formation in the universe occurred [13].

2 Lensing Theory

In this section I provide a short summary of gravitational lensing theory, based on the proceedings of the Saas-Fee Gravitational Lensing course, Kochanek et al. (2006) [14].

2.1 The Lensing Equation

Figure 1 below shows the basic geometry of a gravitational lens. It is assumed that the distances involved are much larger than the size of the source and of the lens, allowing us to use a thin-lens approximation.

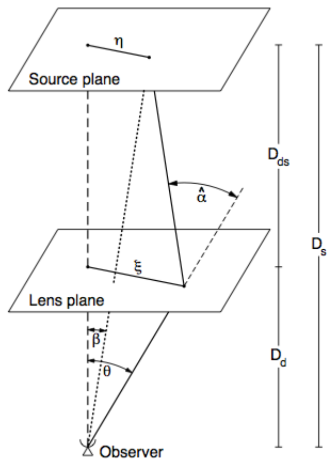

Figure 1: Basic geometry of a gravitational lens for a source in the source plane at distance D_s from the observer, and a deflector (lens) at the lens plane at a distance D_d from the observer, under the thin lens approximation. A source (say a galaxy) is located in the source plane at a distance $\boldsymbol{\eta}$ from a reference line, at a distance D_s from the observer (us on Earth). This corresponds to an angular distance $\boldsymbol{\beta}$. Light travels from the source, intersecting the lens plane at a distance $\boldsymbol{\xi}$ from the reference line, which is at a distance D_d from us. This corresponds to an angular distance $\boldsymbol{\theta}$. The light is deflected by an amount $\hat{\boldsymbol{\alpha}}$. This causes the image to appear shifted by an amount $\boldsymbol{\alpha} = \boldsymbol{\theta} - \boldsymbol{\beta}$, where $\boldsymbol{\alpha}$ is the scaled deflection angle (defined below) (image from Saas-Fee Lectures on Gravitational Lensing [14]).

By assuming small angles, we see that $D_s\boldsymbol{\theta} = D_s\boldsymbol{\beta} + D_{ds}\hat{\boldsymbol{\alpha}}$[1]. Or, dividing by D_s and rearranging the equation, $\boldsymbol{\beta} = \boldsymbol{\theta} - \frac{D_{ds}}{D_s}\hat{\boldsymbol{\alpha}}(\boldsymbol{\xi})$. By noting that $\boldsymbol{\xi} = D_d\boldsymbol{\theta}$, we arrive at the lensing equation,

$$\boldsymbol{\beta} = \boldsymbol{\theta} - \frac{D_{ds}}{D_s}\hat{\boldsymbol{\alpha}}(D_d\boldsymbol{\theta}) \equiv \boldsymbol{\theta} - \boldsymbol{\alpha}(\boldsymbol{\theta}), \tag{3}$$

[1]Throughout this paper bold font indicates a vector quantity

where we define the scaled deflection angle, $\boldsymbol{\alpha}(\boldsymbol{\theta}) \equiv \frac{D_{ds}}{D_s}\hat{\boldsymbol{\alpha}}(\boldsymbol{\xi})$.

2.2 Convergence, Shear, and Magnification

The distortion of images can be described by the Jacobian matrix,

$$J(\boldsymbol{\theta}) = \frac{\partial \boldsymbol{\beta}}{\partial \boldsymbol{\theta}} = \begin{pmatrix} 1-\kappa-\gamma_1 & -\gamma_2 \\ -\gamma_2 & 1-\kappa+\gamma_1 \end{pmatrix}. \tag{4}$$

Here $\kappa(\boldsymbol{\theta})$ is a dimensionless surface mass density, or *convergence*, defined as

$$\kappa(\boldsymbol{\theta}) \equiv \frac{\Sigma(D_d\boldsymbol{\theta})}{\Sigma_{cr}},$$

with $\Sigma(D_d\boldsymbol{\theta})$ the *surface mass density* of the lens and

$$\Sigma_{cr} \equiv \frac{c^2}{4\pi G}\frac{D_s}{D_d D_{ds}}$$

the *critical surface mass density* (see figure 2). The regime of strong lensing is when $\Sigma > \Sigma_{cr}$.

We have also defined the *shear*, $\gamma \equiv \gamma_1 + i\gamma_2 = |\gamma|e^{2i\phi}$. The shear in some sense skews the images (see figure 2).

Equation (4) tells us how the location of the source changes if we change the location(s) of the image(s). If the source is small compared to the scales at which the lens properties change, then the inverse of this matrix is called the magnification tensor,

$$M(\boldsymbol{\theta}) = J^{-1}. \tag{5}$$

This tensor tells us the local mapping from the source to the image plane. The *magnification* (again for a small source) is defined as the determinant of the magnification tensor,

$$\mu \equiv \det\ M = \frac{1}{\det\ J} = \frac{1}{(1-\kappa)^2 - |\gamma|^2}. \tag{6}$$

So we see that for a lens with no shear ($|\gamma| = 0$), that if $\kappa = 1$ ($\Sigma = \Sigma_{cr}$) then the image will be infinitely magnified. Infinite magnification will also occur when $|\gamma|^2 = (1-\kappa^2)$. Of course infinite magnification is unphysical, and the resolution to this problem is in the next section.

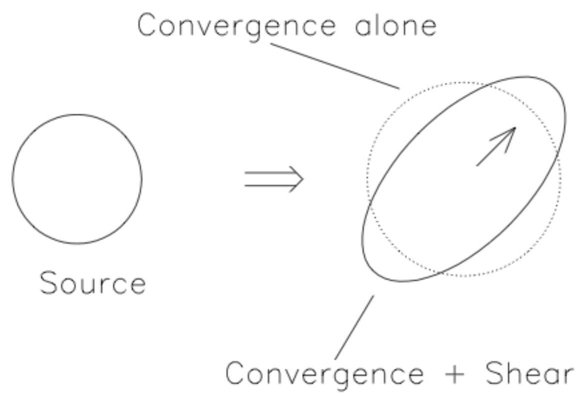

Figure 2: Figure showing effects of convergence and shear. The convergence magnifies (or demagnifies) and the shear skews the images (image from Narayan and Bartelmann's lectures on gravitational lensing [15]).

2.3 Critical Curves and Caustics

As can be seen from equation 6, for certain values of κ and γ the magnification can approach infinity. These values translate to locations in the image plane, called *critical curves*. If these curves are mapped from the image plane to the source plane (via the lensing equation 3) then we get what are called *caustics*. The locations of the images, their parity, magnification, and morphology are determined by the source's location relative to the caustics. If the source lies exactly on a caustic, then it's image will lie exactly on a critical curve, and therefore will theoretically be infinitely magnified. This apparent violation of the conservation of energy is resolved by the fact that for a source to lie *exactly* on a caustic it must be infinitely small. As the size of a source shrinks, eventually the assumption of geometric ray optics breaks down and wave optics must be used. This has been done [14] and the predicted interference pattern has a finite magnification.

There are two different critical curves (and associated caustics), the *tangential* and *radial* curve. As the source approaches a tangential caustic its image will be magnified in the tangential (ϕ) direction along the tangential critical curve and as a source approaches a radial caustic it will be magnified in the radial (r) direction perpendicular to the radial curve.

As shown by Burke [16], lensing always produces an odd number of images. This means that if a source is outside of all the caustics, the lens will produce one image, that is both deflected and distorted. As it crosses a caustic two more images will be created (see figure 3). As it crosses a second caustic five images will be created, and so on.

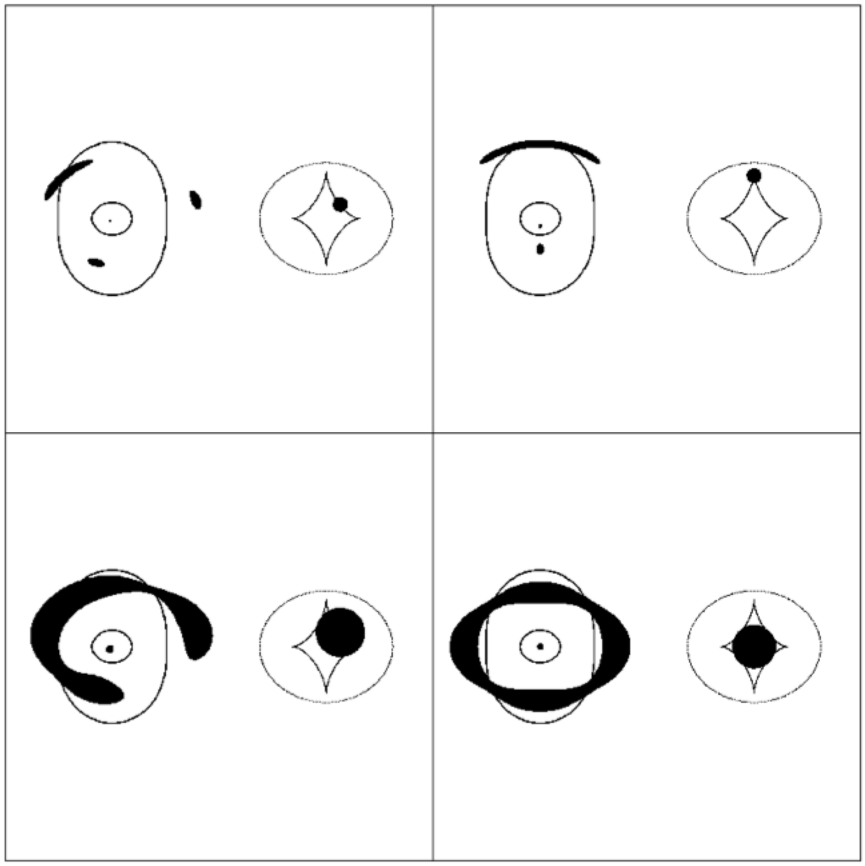

Figure 3: Figure showing relationship between sources, caustics, and multiple images. The right image in each pane shows a source and where is is relative to caustics and the left image in each pane shows the image created by that source. Note that in the top-left pane there is a *merging pair* that is crossing the critical curve. This is one image being turned into two because the source is crossing a caustic (image from Narayan and Bartelmann's lectures on gravitational lensing [15]).

2.4 Parametric vs. Non-parametric Modeling

There are two ways to model a lens–parametric and nonparametric. Parametric modeling is when an analytic function is used to describe the potential. There are many models to choose from, but we use the PIEMD (see appendix). Non-parametric models are different in that the lensing potential is treated as a function of the surface density [14]. These models reconstruct the mass distribution as a map defined on a grid of pixels [17].

2.5 Outline of Lenstool

To model gravitational lenses we use the publicly available software, `LENSTOOL` [17]. This is a program that uses ray tracing to find the best-fit model for a strong gravitational lens. As an example of how the program works, assume that there is a system with multiple images of a galaxy. Lenstool will send rays of light starting from each of the images and compute their positions in the source plane. Depending on the parameters of the model (see below) the light rays will land in different places. A χ^2 is assigned to the scatter between the points. This is done as follows: assume we have a source with position $\boldsymbol{\beta}$. Also assume that this source produces n images θ_i. The light rays traced through the θ_i's land in the source plane at positions β_i with uncertainties σ_i. The χ^2 is calculated by

$$\chi^2_{source} = \sum_{i=1}^{n} \left(\frac{\boldsymbol{\beta} - \boldsymbol{\beta_i}}{\sigma_i} \right)^2 . \tag{7}$$

If the model were perfect then all of the light rays through the multiple images would land at identically the same spot in the source plane and the χ^2 would be identically zero. For each non-perfect model though there will be some scatter between points, and the best-fit model is deemed the one that has the minimum amount of scatter (or equivalently, the χ^2 is minimum for the best-fit model). This is called source plane optimization. In image plane optimization rays of light are sent through the lens back to the source plane, and then sent again through the lens and see where they fall in the image plane. To calculate a χ^2 rays of light are sent from the source plane at the predicted source location and their (n) locations in the image plane θ_i are computed. The formula is

$$\chi^2_{image} = \sum_{i=1}^{n} \left(\frac{\boldsymbol{\theta_i}(\boldsymbol{\beta}) - \boldsymbol{\theta_i}}{\sigma_i} \right)^2 . \tag{8}$$

Again the model that provides the minimum amount of scatter is deemed the best-fit model. This method takes significantly more time to run and therefore is only done after a satisfactory model is obtained with source plane optimization.

3 SDSS J1438+1454

My research has focused on making models for strong gravitational lenses. The rest of this paper will focus on one lens in particular, SDSS J1438+1454 (hereafter SDSS 1438) (see figure 4). The discovery of this lens and a multi-wavelength analysis of the source galaxy are presented in Gladders et al. [18].

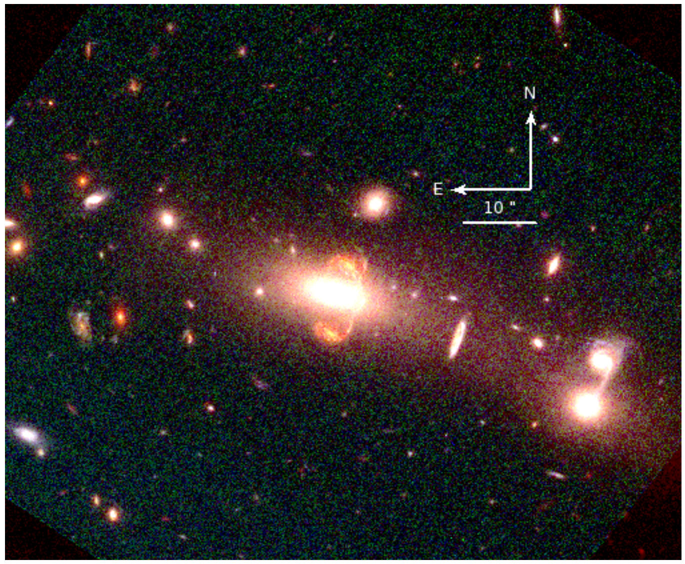

Figure 4: HST image of SDSS 1438. This is a composite image of three filters, centered on: 1400 nm, 814 nm, and 606 nm.

3.1 SGAS Survey

The Sloan Giant Arcs Survey[2] is a survey for cluster- and group-scale gravitational lenses in the Sloan Digital Sky Survey [19] (SDSS). The survey yielded hundreds of lenses [5–7] with a good understanding of its completeness and purity (Gladders et al. in preparation). SGAS clusters have been confirmed through optical follow up using medium and large ground-based telescopes (such as the Nordic Optical Telescope, Gemini). An extensive follow-up campaign provides multi-wavelength observations of all the secure lenses including imaging and spectroscopy of the clusters and the background sources from Gemini North [20], Gemini South, Magellan [11], and imaging with SOAR [21], NOT [22, 23], and Spitzer. As part of this campaign, about 40 of the SGAS clusters were followed up by dedicated HST programs GO13003, GO13337, GO13437, GO13639, GO14230, GO14170 [24–26].

3.2 SDSS J1438+1454

This cluster was selected as a candidate for the SGAS project because with SDSS data the object located $18''.5$ WSW of the BCG strongly resembles evidence of

[2]Michael Gladders, University of Chicago (PI); Keren Sharon, (1); Jane Rigby, NASA Goddard Space Flight Center; Eva Wuyts, Max Planck Institute for Extraterrestrial Physics; Matt Bayliss, Harvard University; Håkon Dahle, Institute of Theoretical Astrophysics; Joe Hennawi, Max Planck Institute for Astronomy; Katherine Whitaker, University of Massachusetts Amherst; Traci Johnson, (1); Rachael Paterno-Mahler, (1); Katherine Murray, (1); Catherine Cerny, (1); and myself, (1). (1): University of Michigan

strong lensing (see figure 4). Follow-up work concluded that it was in fact a cluster-member galaxy, however a reddish tint was noticed around the BCG. With Spitzer observations with IRAC at 3.6 μm and 4.5 μm this red object was seen to be very bright in the infrared an likely to be multiply imaged [18].

We used GALFIT [27] to model the light of the BCG, which was best fit with a multi-component Sérsic profile. We then subtracted the BCG model from the imaging data in each filter, to produce an image with the BCG light removed (see figure 5)[3]

3.3 Hubble Space Telescope Imaging Data

SDSS 1438 was observed by HST Cycle 21 program GO–13437 (PI: Rigby) during three orbits. Imaging with the Advanced Camera for Surveys (ACS) was executed over one orbit on GMT 2014 March 5, in F814W (600 s) and F606W (780 s). Wide Field Camera 3 (WFC3) grism observations were conducted in two different roll angles, one on GMT 2014 March 5 and one on May 30, using the G141 grism (2406 s each), with a F140W imaging frame taken at each roll angle (285 s each). The spectroscopic observations are not used in the lensing analysis. The ACS images were taken with a 3-point line dither using 1000×1000 pixel subraster to manage buffer dumps, resulting in three frames per filter. Since the charge transfer efficiency of the ACS detector is decreasing, post-observation image corrections were applied to individual exposures using the Pixel-based Empirical charge transfer efficiency Correction Software provided by STScI. Individual frames were then combined using AstroDrizzle (Gonzaga at al. 2012) with a pixel scale of $0.''3$ pixel^{-1}, and a drop size of 0.5 (WFC3) and 0.8 (ACS), following Sharon et al. (2015).

All the images were aligned and registered to the same pixel frame as the F140W image.

[3] The GALFIT modeling and image subtraction analysis were conducted by my collaborator M. Gladders. The HST data were reduced by my collaborator Michael Florian.

Figure 5: HST image of SDSS 1438 with BCG light removed. The BCG was obscuring much of the detail and so was removed with a GALFIT program [18]. This is a composite image of three filters centered on: 1400 nm, 814 nm, and 606 nm.

3.4 Constraints

The basic problem in lensing is to solve the lensing equation,

$$\boldsymbol{\beta} = \boldsymbol{\theta} - \boldsymbol{\alpha}(\boldsymbol{\theta}, \boldsymbol{p}), \tag{9}$$

where $\boldsymbol{p}$ represents the model parameters (see below). To solve equation 9 we need at least as many constraints as free parameters. To get the constraints we use the RA and DEC of multiply imaged parts of the galaxy. Looking at the top image of the lensed galaxy in figure 5 we see that is a spiral galaxy with a yellow central core and red spiral arms. In the spiral arms we see several white knots. These are star-forming regions of the source. They are easily distinguishable in each image and so were used as constraints, along with the yellow core (see figure 6). Table 1 below is a table listing all constraints used.

Constraints			
Symbol	**Image ID**	**R.A.(J2000) [degrees]**	**Decl.(J2000) [degrees]**
Magenta Circle	10.1	219.68704	14.904572
	10.2	219.68696	14.903430
	10.3	219.68777	14.901929
Blue Diamond	11.1	219.68717	14.904282
	11.2	219.68703	14.903652
	11.3	219.68787	14.901701
Blue Circle	12.1	219.68686	14.904191
	12.2	219.68679	14.903699
	12.3	219.68764	14.901701
Blue Square	13.1	219.68662	14.904108
	13.2	219.68660	14.903708
	13.3	219.68737	14.901716
Cyan Square	14.1	219.68677	14.904353
	14.2	219.68672	14.903530
	14.3	219.68752	14.901806
Cyan Circle	15.1	219.68684	14.904579
	15.2	219.68679	14.903349
	15.3	219.68756	14.901952
White Circle	16.1	219.68641	14.904516
	16.2	219.68650	14.903197
	16.3	219.68707	14.902029
Red Square	17.1	219.68747	14.904875
	17.2	219.68833	14.903578
	17.3	219.68816	14.902269
Red Circle	18.1	219.68773	14.904724
	18.2	219.68843	14.903754
	18.3	219.68833	14.902189
Yellow Circle	19.1	219.68685	14.904857
	19.2	219.68690	14.903173
	19.3	219.68753	14.902201
Green Circle	20.1	219.68738	14.904508
	20.3	219.68804	14.901883
Pink Circle	21.1	219.68824	14.904039
	21.2	219.68785	14.904465
Orange Circle	22.1	219.68731	14.904751
	22.2	219.68819	14.903645
Gold Square	23.1	219.68716	14.904693
	23.2	219.68796	14.903606

Table 1: Table of constraints. The convention for the image IDs is that the number to the left of the decimal point corresponds to a particular set of images and the number after the decimal point corresponds to a specific image within that set.

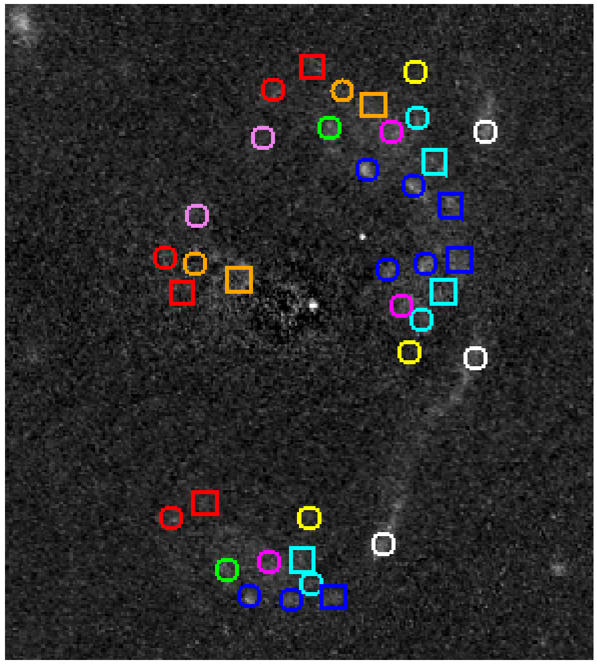

Figure 6: Constraints used for lens model, over plotted on an image of the lens in the F606W filter, after having the light of the BCG modeled and substracted. Similar symbols and colors represent multiple images of the same source position (see table 1.)

3.5 Parameters

The number of free parameters is determined by which mass profile we use to model the halos and how many halos we use. All the halos are modeled as pseudo-isothermal ellipsoidal mass distributions (PIEMD, see appendix A), which has seven free parameters: center point x, center point y, ellipticity e, position angle θ , core radius r_{core}, cut radius r_{cut}, and velocity dispersion σ. Standard practice is to use one halo that represents the cluster as a whole. We allow all its parameters to vary, with the exception of the cut radius: we fix the cut radius at 1000 *kpc* because this parameter is not well constrained. This is because the cut radius is well outside the outermost arc and thus cannot be constrained by the lens model. We add another halo to represent the brightest cluster galaxy (BCG) and allow its parameters to vary as well. However for the BCG we fix its RA and DEC because these are known quantities. We fix the cut radius for the BCG at 300 *kpc*. Additional halos can be added as needed depending on the complexity of the lens and the availability of lensing constraints. In addition to the optimized halos we also allow contributions to the mass from other cluster-member galaxies. Cluster-member galaxies were identified from the HST photometry by their F814W-F140W color on a colormagnitude diagram. The positions, ellipticity, and position angle were fixed to their observed values, and the PIEMD profile parameters, r_{cut}, r_{core}, and σ, were scaled to their F140W luminosity using scaling relations, following Limousin et al. (2005) [28].

3.6 Results

3.6.1 The Lens Model

The best-fit model is obtained by an MCMC optimization sampling 1000 different models. We set priors and ranges for each parameter that varied. As the model improved and we consistently produced similar results we tightened the constraints on the parameters. With six free parameters for the cluster halo and four for the BCG halo, there are ten free parameters in total for this model. We have identified 38 different knots which gives 76 constraints.

This model was run through both source-plane and image-plane optimizations, the χ^2 of the best model in the image plane being 1.72. Figure 7 shows the critical curves and caustics of the best-fit model for a source at $z = 0.816$. The critical curves represent the locations in the image plane where we would theoretically have an infinite magnification. If these curves are mapped to the source plane we get what are called caustics. The images change parity when they are on either side of a critical curve (see figure 7), in other words they have mirror symmetry. The critical curves bisect the image plane, and the images of the galaxy appear with the symmetry and parity we expect.

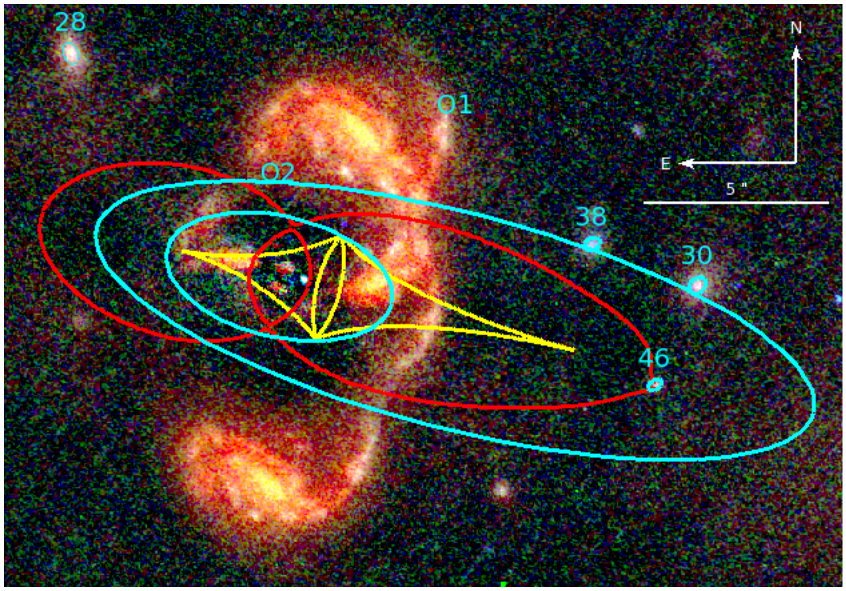

Figure 7: The best-fit lens model of SDSS J1438+1454. Cyan ellipses represent the locations of mass halos. O1 is the dark matter halo, O2 is the BCG halo, and the numbers correspond to cluster member galaxies ranked in descending order of their flux, starting with the BCG. The red curves are the critical curves, drawn for a source at $z = 0.816$ and the yellow curves are the caustics. The dark matter halo is $5''$ offset from the BCG in the direction of the second and third brightest cluster galaxies, which contribute significantly to the mass distribution.

Figure 8 is a collection of 2D histograms where every free parameter is plotted against every other free parameter. The values come from chains of parameters in the MCMC sampling and the color gradient is such that redder areas represent higher densities of points. We find that the x and y parameters are anti-correlated, so that as the center of the cluster halo is moved along the SW-NE diagonal the model does not change appreciably. The correlation between σ and r_{core} is a consequence of our choice of the PIEMD for a mass profile (see appendix A). Table 2 shows the values for each parameter from the best-fit model. The uncertainties for the values in table 2 are calculated by finding a 68% confidence interval centered on the mean and then finding the difference between the value at the upper and lower bounds and the best-fit value.

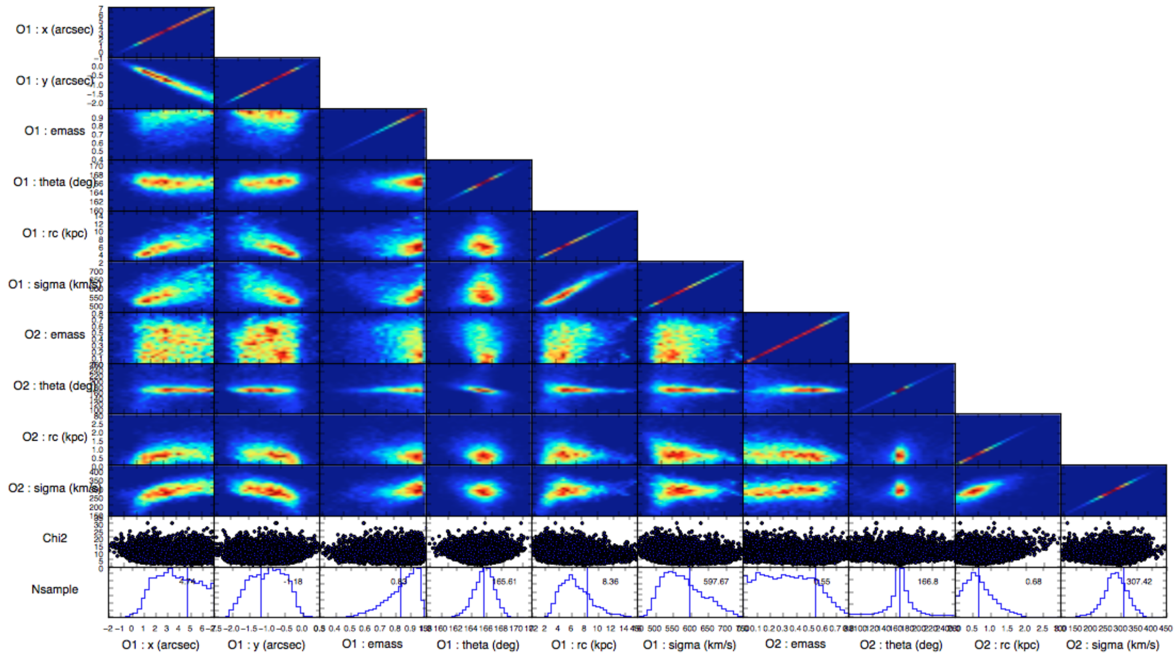

Figure 8: 2D histogram showing the free parameters plotted against each other. The x and y of the cluster are correlated, meaning that there is a degeneracy in the lens model. If the cluster center point is moved in the x direction and the correlated amount in the y direction, then the model would be just as good. The correlation between the cluster core radius and the cluster velocity dispersion is a result of using the PIEMD for the potential, where those two parameters' correlation is built in.

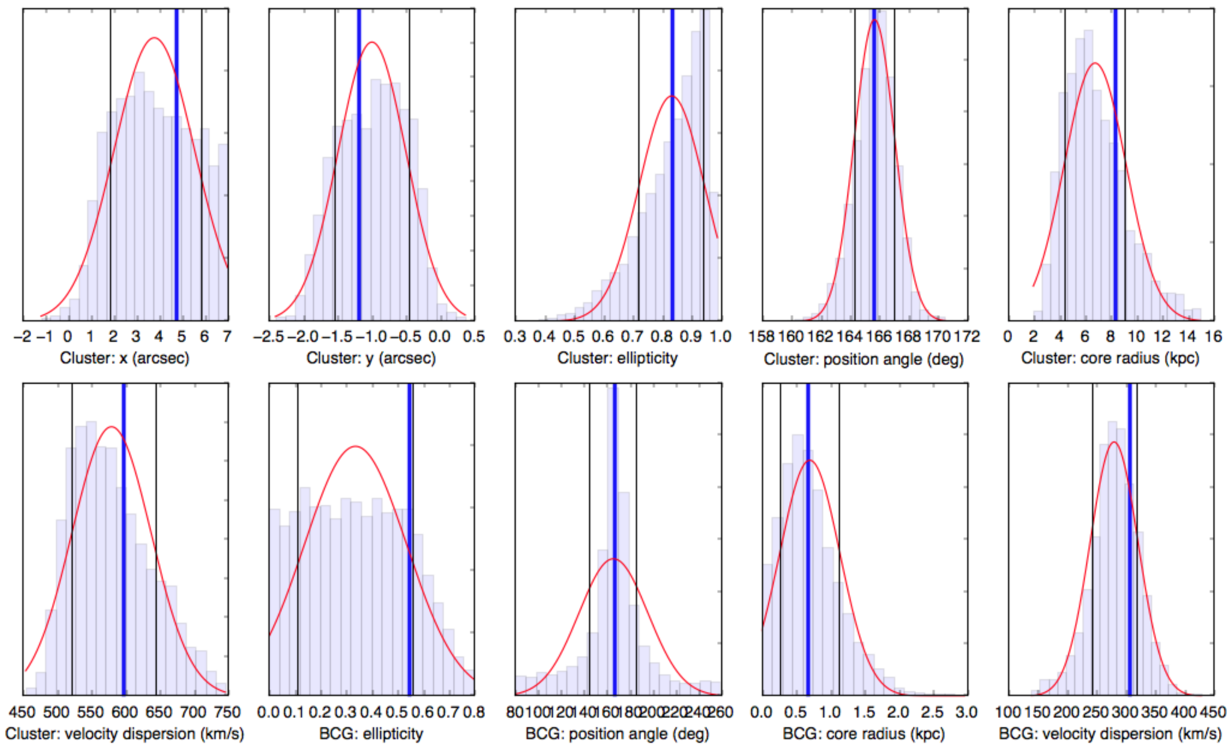

Figure 9: These histograms show the number of times each model had each parameter. The blue lines are the best-fit value and the black lines enclose 68% of the models. The red curve is a best-fit Gaussian, which may not actually represent the data but can be useful nevertheless. See table 2 for numbers.

Best-Fit Values		
Parameter	Cluster	BCG
R.A. ["]	$4.74^{+1.10}_{-2.90}$	0
Decl. ["]	$-1.18^{+0.73}_{-0.37}$	0
e	$0.83^{+0.11}_{-0.11}$	$0.55^{+0.01}_{-0.44}$
θ [°]	166^{+1}_{-1}	167^{+19}_{-22}
r_{core} [kpc]	$8.36^{+0.73}_{-3.96}$	$0.68^{+0.45}_{-0.40}$
σ [km/s]	598^{+47}_{-76}	307^{+13}_{-64}

Table 2: Best-fit values from the image plane optimization. The R.A. and Decl. of the BCG are fixed and the observed location, R.A. = 219.68768°, and Decl. = 14.903482°. The position of the cluster halo is measured relative to the BCG. θ is measured north of west, and the ellipticity of the projected mass density is $e = (a^2 - b^2)/(a^2 + b^2)$.

3.6.2 The Cluster Mass

The best-fit model is translated from a 3D mass density to a projected mass density by integrating out the line-of-sight variable, leading to equation 11. We calculate the projected mass density of the cluster from the best-fit model (see figure 10) and then sum that over a disk of radius $9''(\approx 34\ kpc)$ centered on the BCG. We choose that radius because strong lensing only constrains the mass out to furthest arc. Therefore, the mass quoted here is a mass of the *core* of the cluster, not the total mass. The total mass of the cluster would be best measured by weak lensing or other mass proxies, and is beyond the scope of this work. Nevertheless, extrapolation of the strong lensing mass out to 500 kpc ($\sim 135''$) yields a total enclosed mass of $1.06 \times 10^{14}\ M_{\odot}$. We note that this number has a large uncertainty, due to the inability of strong lensing alone to constrain the mass outside of the strong lensing region.

We calculate the uncertainties by going through a representative sample from the MCMC sets of parameters (in this case all of the models) and calculating the mass of the cluster for each one. In figure 11 we plot the mass of the cluster as calculated from parameter sets from all the steps of the MCMC sampling. The best-fit enclosed mass within 9 arcsec (34 kpc) is $6.08^{+0.25}_{-0.65} \times 10^{12}\ M_{\odot}$. The uncertainties are estimated as 1σ as sampled by the MCMC process.

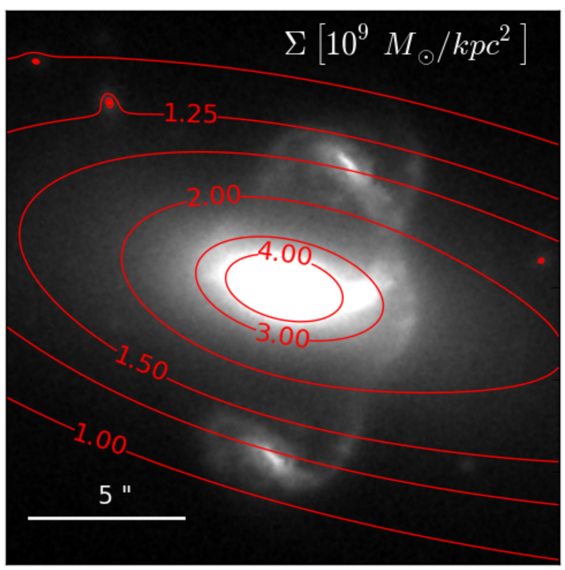

Figure 10: Surface mass density contour plot.

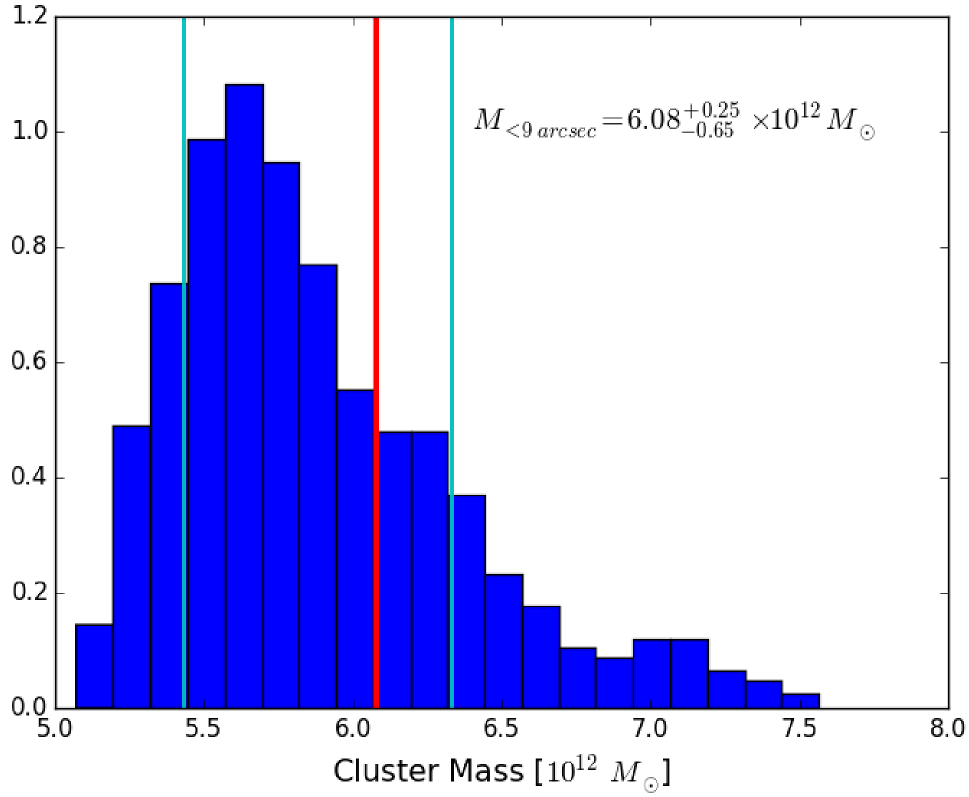

Figure 11: Histogram showing 1000 different models with slightly varied parameters in 20 bins. The red line is the location of the best model. The two cyan lines contains 68% of the models. The mass is calculated within a 9 arcsecond radius ($\approx 34\ kpc$) from the BCG. This is because strong lensing only constrains the mass out to the distance of the furthest lensed image.

3.6.3 Magnification

Figure 12 shows the magnification contours from the best-fit model. We find that the magnification is not constant along the galaxy, but changes by about a factor of three across one image (about $5\farcs'' \approx 19\ kpc$). At the core of the top image the magnification is about 3.5, for the bottom it is about 2.75, and for the bisected image it is about 2. The estimated total magnification, taken by summing the areas of each image and dividing that by the area of the galaxy, is $\mu = 12.96$.

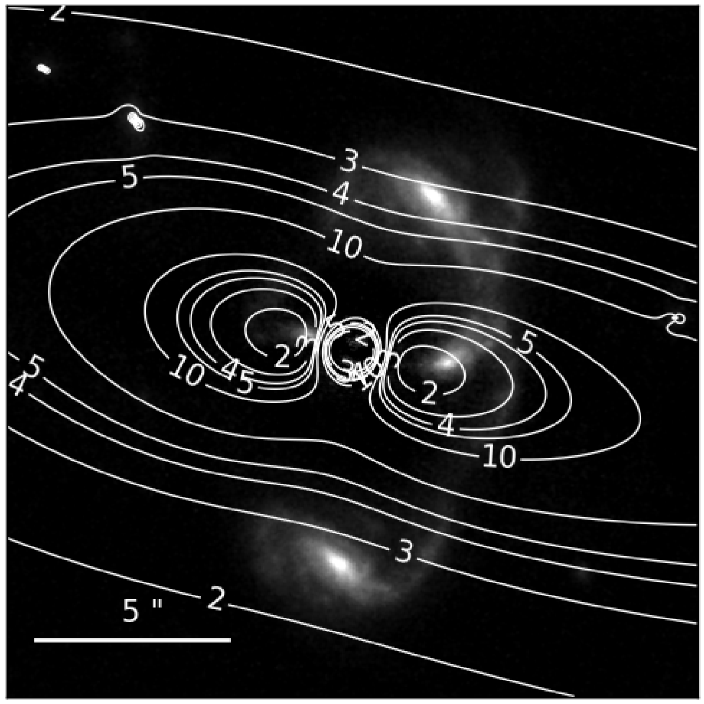

Figure 12: Magnification contours.

4 Discussion

The mass of the cluster is about as massive as a small group of galaxies [29]. This is in line with the number of galaxies reported in Gladders et. al. [18] of $N_{gals}^{weighted} = 9.735$. The center of the cluster halo is 5.″05 WSW from the center of the BCG halo. It is expected in small galaxy groups that the BCG would be offset from the center of mass of the group [30]. This is consistent with the light distribution of the cluster, as can be seen in figure 4. The velocity dispersion that was reported in Gladders et. al. [18] of 318 ± 111 km/s is in good agreement with our best-fit value.

This kind of magnification allows our collaboration to study star formation in the source galaxy in detail that would be unattainable without lensing. The typical magnification of individual emission knots/star-forming regions is a factor of 3-5. This helps us study individual star forming regions in a galaxy at $z = 0.8$.The angular size of the source galaxy, unmagnified, is 2.″53(≈ 19 kpc).

In good conditions, ground-based resolution is $0\farcs6$, therefore this galaxy would cover at best up to four non-overlapping resolution elements, dominated by the bulge. With the magnification boost, even ground observations can resolve more than ten regions in this galaxy and thus resolve its structure.

5 Future Work

By identifying multiple images in a strong gravitational lens we were able to develop a model for the lens. With this model we were able to get the mass of the cluster core, the magnification it provides, and the actual location of the sources. The next step is to hand this model to the next person in the pipeline of the SGAS project. Using this model they will be able to study the star-forming knots in the lensed cluster.

Grism spectroscopy of SDSS J1438+1454 was recently obtained by HST. My collaborators are reducing the Grism observation and analyzing the data (PI: Rigby) and will use these observations to study SDSS J1438+1454, a cool, luminous infrared galaxy at z=0.8, and learn about the evolution of luminous infrared galaxies from z=1 to present day. In particular, they will measure the current star formation rate and its distribution in the galaxy, star formation history, and stellar mass. To translate all of these properties from the observed frame to the intrinsic, unlensed frame, one needs a good understanding of the magnification – since they all scale linearly with the magnification. Therefore, the magnification map that I calculated and presented in this thesis will be a critical and indispensable input to understanding the physical properties of this galaxy in particular, and through that, study the evolution of its population across cosmic time.

A Pseudo Isothermal Ellipsoidal Mass Distribution-PIEMD

We use parametric modeling (vs. non-parametric) and this means that we assume that the gravitational potential can be modeled with an analytic function. There are many out there, but some of the most common are the Navarro-Frank-White (NFW), the singular isothermal sphere (SIS), a power law with a core radius, and a Sérsic. In fact the SIS is just a special case of the PIEMD with a vanishing core radius. The models all assume a three-dimensional mass distribution, $\rho(r) = f(r)$. However we assume that the lens is very thin compared to the distances between it and the source and between it and us. Therefore lensing effectively occurs on a two-dimensional plane in the sky, so the quantity of interest is actually the integral of $\rho(r)$ over the line of sight variable yielding the surface mass density, called $\Sigma(R)$, with R being a two-dimensional radial coordinate in the plane of the sky. The analytic form of the PIEMD is

$$\rho(r) = \frac{\rho_0}{(1 + r^2/r_{core}^2)(1 + r^2/r_{cut}^2)}, \tag{10}$$

with r_{core} being the core radius and r_{cut} being the cut radius, and $r_{cut} > r_{core}$. Near the center, $r \ll r_{core} < r_{cut}$, so $\rho(r) \approx \rho_0$. When $r_{core} < r < r_{cut}$, the distribution falls of as r^{-2} [28]. Far away, $r \gg r_{cut}$ so the distribution falls off as r^{-4}, which is typical of elliptical galaxies [28]. Integration of (10) over the line of sight coordinate yields [28]

$$\Sigma(R) = \frac{\sigma_0^2 r_{cut}}{2G(r_{cut} - r_{core})} \left(\frac{1}{\sqrt{r_{core}^2 + R^2}} - \frac{1}{\sqrt{r_{cut}^2 + R^2}} \right), \tag{11}$$

where σ_0 is the central velocity dispersion and is related to ρ_0 by

$$\rho_0 = \frac{\sigma_0^2}{2\pi G} \left(\frac{r_{cut} + r_{core}}{r_{core}^2 r_{cut}} \right). \tag{12}$$

References

[1] Soares, D. S. L. 2005, arXiv:physics/0508030

[2] Einstein, A. 1915, Sitzungsber. preuss.Akad. Wiss., vol. 47, No.2, pp. 831-839, 1915, 47, 831

[3] http://www.amnh.org/education/resources/rfl/web/essaybooks/cosmic/p_zwicky.html

[4] Gladders, M. D., et al., in preparation

[5] Bayliss, M. B., Gladders, M. D., Oguri, M., et al. 2011a, ApJL, 727, L26

[6] Bayliss, M. B., Hennawi, J. F., Gladders, M. D., et al. 2011b, ApJS, 193, 8

[7] Hennawi, J. F., Gladders, M. D., Oguri, M., et al. 2008, ApJ, 135, 664

[8] Wuyts, E., Rigby, J. R., Gladders, M. D., et al. 2012, ApJ, 745, 86

[9] Sharon, K., Gladders, M. D., Rigby, J. R., et al. 2012, ApJ, 746, 161

[10] Rigby, J. R., Bayliss, M. B., Gladders, M. D., et al. 2014, ApJ, 790, 44

[11] Rigby, J. R., Bayliss, M. B., Gladders, M. D., et al. 2015, ApJL, 814, L6

[12] Bordoloi, R., Rigby, J. R., Tumlinson, J., et al. 2016, MNRAS, 458, 1891

[13] Rigby, J. R., Wuyts, E., Gladders, M. D., Sharon, K., & Becker, G. D. 2011, ApJ, 732, 59

[14] Meylan, G., Jetzer, P., North, P., et al. 2006, Saas-Fee Advanced Course 33: Gravitational Lensing: Strong, Weak and Micro,

[15] Narayan, R., Bartelmann, M, Lectures on Gravitational Lensing. arXiv:astro-ph/9606001

[16] Multiple Gravitational Imaging by Distributed Masses, 1981

[17] Jullo, E., Kneib, J.-P., Limousin, M., et al. 2007, New Journal of Physics 9, 447.

[18] Gladders, M. D., Rigby, J. R., Sharon, K., et al. 2013, ApJ, 764, 177

[19] York, D. G., Adelman, J., Anderson, J. E., Jr., et al. 2000, AJ, 120, 1579

[20] Bayliss, M. B., Hennawi, J. F., Gladders, M. D., et al. 2011, ApJS, 193, 8

[21] Bayliss, M. B. 2012, ApJ, 744, 156

[22] Dahle, H., Gladders, M. D., Sharon, K., et al. 2013, ApJ, 773, 146

[23] Dahle, H., Gladders, M. D., Sharon, K., Bayliss, M. B., & Rigby, J. R. 2015, ApJ, 813, 67

[24] Sharon, K., Gladders, M. D., Rigby, J. R., et al. 2014, ApJ, 795, 50

[25] Tremblay, G. R., Gladders, M. D., Baum, S. A., et al. 2014, ApJL, 790, L26

[26] Bayliss, M. B., Rigby, J. R., Sharon, K., et al. 2014, ApJ, 790, 144

[27] Peng, C. 2010, Bulletin of the American Astronomical Society, 42, 229.09

[28] Limousin, M., Kneib, J.-P., & Natarajan, P. 2005. MNRAS, 356, 309

[29] Han, J., Eke, V. R., Frenk, C. S., et al. 2015, MNRAS, 446, 1356

[30] George, M. R., Leauthaud, A., Bundy, K., et al. 2012, ApJ, 757, 2